Journal of Materials Chemistry C

Accepted Manuscript

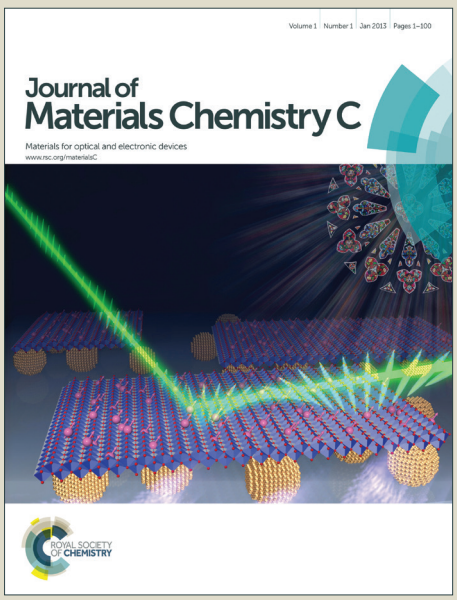

ROYAL SOCIETY OF CHEMISTRY

www.rsc.org/materialsC

Cite this: DOI: 10.1039/c0xx00000x

www.rsc.org/xxxxxx

ARTICLE TYPE

Chiral nematic mesoporous films of Y_2O_3:Eu^{3+} with tunable optical properties and modulated photoluminescence

Guang Chu,[a] Wen Xu,[b] Dan Qu,[a] Yu Wang,*[a] Hongwei Song [b] and Yan Xu*[a]

Received (in XXX, XXX) Xth XXXXXXXXX 20XX, Accepted Xth XXXXXXXXX 20XX

DOI: 10.1039/b000000x

Chiral nematic mesoporous yttrium oxide films are attractive for the design of new optical devices. The free-standing chiral nematic mesoporous films of Y_2O_3:Eu^{3+} are assembled by a hard-templating method using nanocrystalline cellulose-templated silica. The Y_2O_3:Eu^{3+} films with tunable optical properties are capable of modulating the spontaneous emission of Eu^{3+} ions and exhibit interesting photoluminescent properties.

Introduction

Photonic crystals have attracted considerable attention due to their unique spatial periodicity in dielectric media on the scale of optical wavelength,[1-4] that render them potential applications as frequency filters, waveguides, signal modulators, optical switches and fluorescent sensors, *etc*.[5-9] Incorporation of luminescent species into a photonic crystal could modulate their emission spectra due to the photonic stop band (PSB). Specifically, the fluorescence of luminescent species can be suppressed inside the band gap and enhanced near the edges due to high photonic density of states (DOS), the group velocity could be reduced at the band edges, and the resulting long dwelling time of emitted photons could strengthen stimulated emission.[10-13] Among various luminescent species, trivalent rare earth ions with 4*f*-4*f* inner-shell transitions hold exciting implications for maximizing the photonic crystal effects due to their narrow spontaneous emission lines and long decay time constants compared to organic dyes and quantum dots.[14-18] The rare earth doped oxides with three dimensional photonic crystal structures show interesting modulation effect on photoluminescence properties.[15, 18, 19]

Chiral nematic liquid crystals are one-dimensional chiral photonic crystals in which mesogens are arranged in a helical order. The helical organization of a chiral nematic crystal induces angle-dependent selective reflection of circularly polarized light, resulting in iridescence when the helical pitch is in the order of wavelength of visible light.[20] Since Voigt's report on the alteration of emission intensity near the PSB, considerable efforts have been devoted to understanding the changes in fluorescence intensity and polarization in the region of the stop band of chiral nematic photonic crystals.[21-24] Chiral nematic polymeric networks incorporating dyes have been used as photonic band edge lasers.[25] Prior work shows that chiral nematic mesoporous silica incorporating silver[26] and CdS quantum dots[27], and chiral nematic zirconia incorporating rare earth ions[28] exhibit interesting optical properties and potential applications in polarizing mirror reflective displays. For this reason, it is worth exploring the modulation effects of chiral nematic structure on the photoluminescence properties of rare earth ions.

Here, we report the fabrication of chiral nematic mesoporous films of Y_2O_3:Eu^{3+} and their intriguing photoluminescence properties. The chiral nematic mesoporous films of Y_2O_3:Eu^{3+} with tunable helical pitch, designated as CNMY, were fabricated by a hard-templating approach using chiral nematic SiO_2 (CNMS) films with different helical pitches as template. The CNMS films were prepared by replicating the chiral nematic assembly of nanocrystalline cellulose through an evaporation-induced self-assembly pathway followed by calcination.[20] The free-standing films of CNMY with tunable helical pitch show strong birefringence. To the best of our knowledge, these are the first rare earth oxides doped with Eu^{3+} that combine mesoporosity with chiral nematic ordering to produce tunable photonic properties and intriguing luminescent properties. Evident difference has been observed for the CNMY films between the spontaneous emission of Eu^{3+} under linearly polarized excited light and unpolarized excited light. Such phenomenon is closely associated with the variation of both structural anisotropy and the local density of states of the chiral nematic mesoporous structures of CNMY. The current work provides primary information that the integration of chiral nematic rare earth oxides with the luminescent rare earth ions renders unique photoluminescence properties that could be useful in the design and fabrication of new optical devices.

Experimental Section

Materials

All Chemicals were used as received without further purification. Tetramethyl orthosilicate (TMOS, 98%), europium nitrate hexahydrate ($Eu(NO_3)_3{\cdot}6H_2O$, 99.9%) and yttrium nitrate hexahydrate ($Y(NO_3)_3{\cdot}6H_2O$, 99.9%) were purchased from Aladin Industry Corporation. Cellulose cotton pulp board was purchased from Hebei Paper Group of China.

Fabrication of CNMY-n films

The preparation of nanocrystalline cellulose and chiral nematic mesoporous SiO_2 (CNMS) films was accomplished according to the reported procedures,[20, 29] with the experimental details given

in Electronic Supplementary Information (ESI). The CNMY films containing 2 mol% of Eu^{3+} ions were prepared by dipping the CNMS films in a freshly prepared solution of $Y(NO_3)_3$ and $Eu(NO_3)_3$ ($Y(NO_3)_3$:$Eu(NO_3)_3$ molar ratio = 49:1, 4M) for 2 h. The salt loaded CNMS film was washed with water to remove the excess ions on the surface of the CNMS film. Next, the impregnated films were dried at 100 °C in air for 1 h, followed by calcination at 600 °C for 6 h at a heating rate of 2 °C·min^{-1}. This procedure was repeated four times in total to ensure sufficient pore loading of CNMS. The calcined composite films were treated with 2 M $NaOH_{(aq)}$ at ambient temperature for 12 h to selectively remove silica, washed thoroughly and air-dried, giving rise to the CNMY films. CNMY containing 2 mol% of Eu^{3+} and varying helical pitch were denoted as CNMY-n where n = 1-3. For the purpose of comparison, reference samples were prepared by grinding CNMY-n to destroy the chiral nematic ordering, designated as REF-n (n = 1-3).

Characterization

Surface morphology was characterized using JEOL-6700 F field emission scanning electron microscope (SEM) at an accelerating voltage of 3 KV and a FEI Tecnai G2S-Twin transmission electron microscope (TEM) with a field emission gun operating at 200 KV. Energy dispersive X-ray (EDX) analysis was performed using a JOEL-IE350 probe. Powder X-ray diffraction (XRD) patterns were recorded on a Rigaku D/Max 2550 X-ray diffractometer (Cu K radiation, λ = 1.5406 Å). UV-visible spectra were carried out on a Shimazu UV-1800 UV-Visible spectrophotometer with a range of 200-1100 nm. Circular dichroism (CD) spectra were recorded on a BioLogic MOS-450 spectropolarimeter and the samples were mounted normal to the beam. Polarized optical microscopy (POM) was conducted on Olympus BX51-P microscope with images taken by polarizers in a perpendicular arrangement. Nitrogen adsorption studies were performed at 77 K using a Micromeritics ASAP 2420. The angle dependent emission spectra were recorded at room temperature using a FluoroMax-4 fluorescence spectrophotometer (Horiba Scientific) equipped with a 450 W Xe-arc lamp. Fluorescence dynamics and emission spectra by excited polarized lights were investigated by a Continuum Precision II 8000 laser system consisting of an Nd:YAG pump and a tunable OPO laser. A linearly polarized light is obtained by insert a polarization beam splitter (OBPS20-0406, 450-680 nm) in the optical path.

Results and Discussions

General features of the CNMY films

The CNMY-n films were prepared by using CNMS-n as hard templates (Scheme 1). Typically, an aqueous solution containing $Y(NO_3)_3$ and $Eu(NO_3)_3$ with Y:Eu = 49:1 was loaded into the mesopores of CNMS-n using the incipient wetness method. Silica template was removed from final composite films using alkaline solution, resulting in free-standing mesoporous films of CNMY-n with different helical pitches. The chiral nematic organization, crystal structures and pore profile of CNMY-n are characterized using SEM, XRD and nitrogen adsorption-desorption isotherms.

CNMS-1 and CNMY-1 are used as representatives for ease of discussion. The ordered helical arrangement is observed in the SEM images of CNMS-1 and CNMY-1 (Figure 1a-1b), confirming chiral transfer from CNMS-1 to CNMY-1. The repeating distance in the order of several hundred nanometers and anti-clockwise twisting morphology are evidenced by SEM,

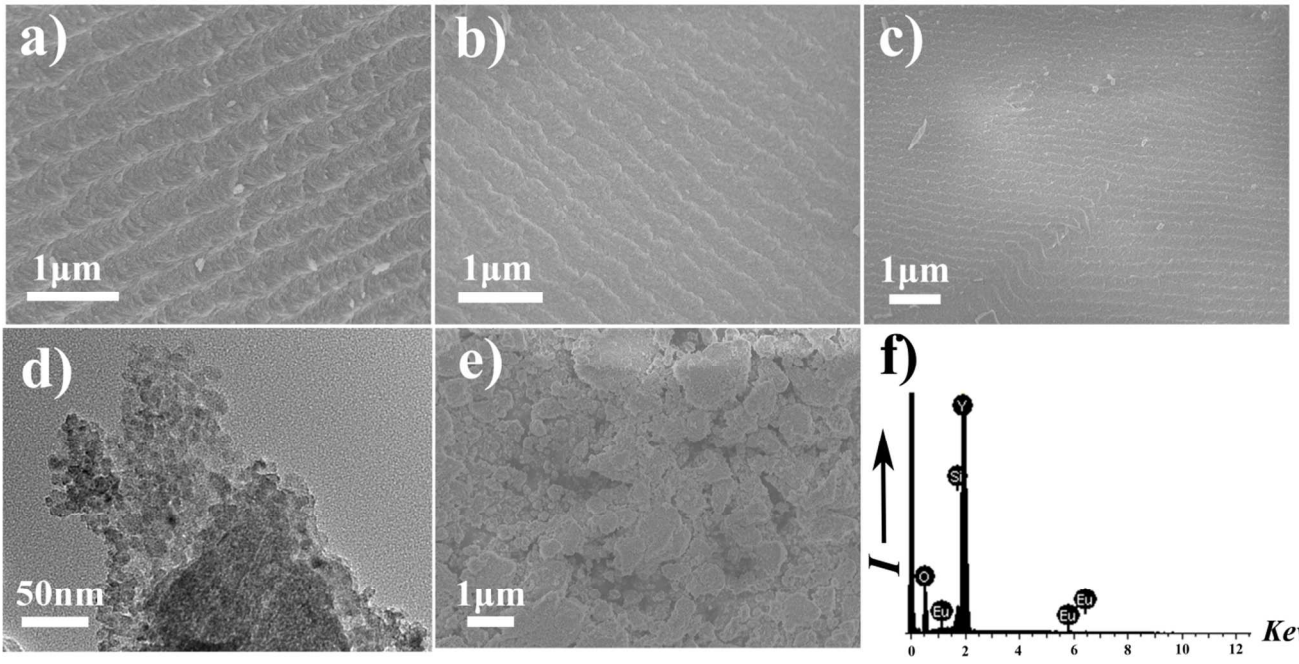

Figure 1. SEM and TEM images of CNMS-1, CNMY-1 and REF-1. (**a**) A cross-sectional view of CNMS-1 by high magnification SEM revealing a helical organization. (**b**) A cross-sectional view of CNMY-1 by high magnification SEM confirming the chiral transfer from the template to the product. (**c**) Top view of CNMY-1 by low magnification SEM. (**d**) Close packing of Y_2O_3:Eu^{3+} nanoparticles in CNMY-1 by high magnification TEM. (**e**) The absence of periodic organization in REF-1 by SEM. (**f**) EDX analysis of CNMY-1 showing a trace amount of Si.

Cite this: DOI: 10.1039/c0xx00000x

www.rsc.org/xxxxxx

ARTICLE TYPE

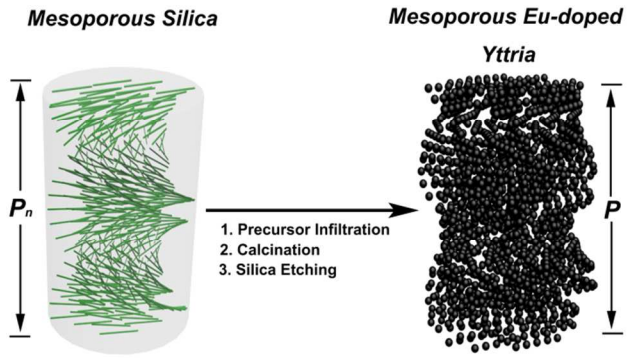

Scheme 1. A schematic diagram of the fabrication of CNMY-n with varying helical pitch by a hard templating method.

revealing the helical pitch of chiral nematic phase and the left-handed helical organization in CNMY-1 (Figure 1b). The top surface of CNMY-1 is relatively smooth, and a layered structure with defects arising from changes in the direction of helical axis of the chiral nematic phase suggests long-range ordering (Figure 1c). TEM image shows that CNMY-1 consists of globular nanoparticles of uniform sizes and stacked layers (Figure 1d). It is possible to organize Y_2O_3:Eu^{3+} nanoparticles into chiral nematic mesoporous structure by replicating CNMS-n with multi-length helical and scalar structural features.[30] Crushing CNMY-1 causes a loss of the chiral nematic ordering as indicated by SEM (Figure 1e). The elemental analyses based on EDX shows that CNMY-1 contains 65.41 wt% of Y, 31.13 wt% of O, 1.13 wt% of Eu and 2.34 wt% of Si (Figure 1f), suggesting that majority of silica has been removed.

The XRD patterns of CNYM-n are shown in Figure 2. The peaks at 29.12°, 33.76°, 48.48°, and 57.68° can be indexed to the (222), (400), (440) and (622) reflections of cubic Y_2O_3 phase (JCPDS 73-1334). No crystalline impurities relating to Eu_2O_3 are detected, confirming that Eu^{3+} ions have been doped into the lattice structure of Y_2O_3. The peak positions on the XRD patterns of CNMY-n are almost identical, suggesting that CNMY-n with different helical pitches have the same crystal structure. The average size of CNMY-1 nanoparticles is around 8 nm based on the Scherrer equation, which is in agreement with the observation based on TEM (Figure 1d).

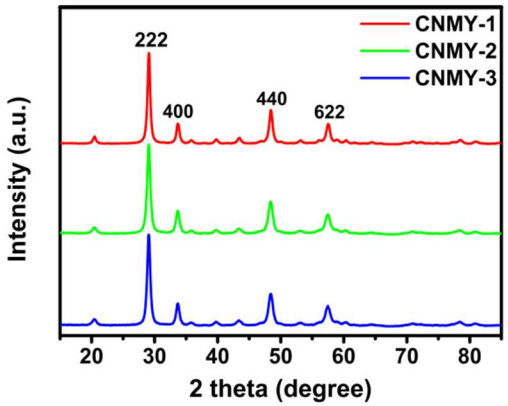

Figure 2. XRD patterns of CNMY-n (n=1-3) showing the cubic structure and absence of crystalline impurity.

The CNMY-n films are mesoporous with narrow pores based on the Barrett-Joyner-Haldenda (BJH) model as revealed by nitrogen adsorption studies (Figure S1, Table S1). The CNMY-n films exhibit a typical type IV adsorption isotherm with H2 hysteresis loop in the range of P/P_0 = 0.4-0.9. The Brunauer-Emmett-Teller (BET) surface areas and pore volumes of CNMY-n are in the range of 70-150 m^2g^{-1} and 0.20-0.30 cm^3g^{-1}, respectively (Table S1). It is worth mentioning that the CNMS-n templates contain similar narrow mesopores, however, their BET surface areas and pore volumes are significantly greater than the corresponding CNMY-n films (Table S1). Apparently, alkaline treatment doesn't destroy the mesoporosity of CNMY-n (Figure S2), and the reduction in the BET surface area might be attributed to the smaller occupation ratio of SiO_2 in the CNMS-n films. The characteristics of the isotherms of CNMS-n and CNMY-n suggest that nanoparticles are arranged in layered structures.[31, 32]

The CNMY films show strong birefringence and domains with different orientations by POM, indicating the anisotropy of the materials (Figure 3a-3c).[33] The color of the CNMY-n films change from red to blue with the reflection peaks blue-shifted by approximately 410 nm from CNMY-1 to CNMY-3 that gives iridescent CNMY-n reflecting light at different wavelengths across the entire visible spectrum. CD spectrum shows a positive signal with a peak at the wavelength of 752 nm for CNMY-1, 568 nm for CNMY-2 and 366 nm for CYMN-3, demonstrating that the observed colors arising from the selective reflection of left-handed polarized light (Figure 3d).[34]

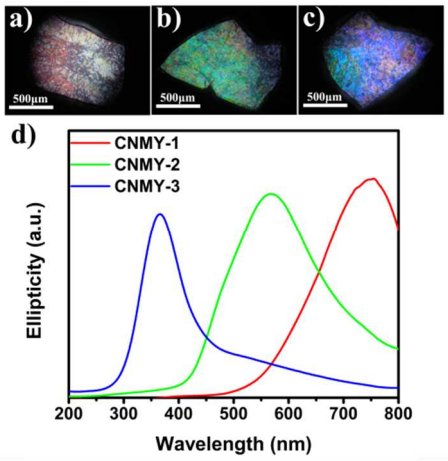

Figure 3. POM images of chiral nematic mesoporous films of CNMY-n: (**a**) CNMY-1, (**b**) CNMY-2 and (**c**) CNMY-3. (**d**) CD spectra of CNMY-n (n=1-3), showing the tunability and the left-handed helical organization of the films.

Photoluminescence and decay dynamics of the CNMY-n films

The photoluminescence properties of the CNMY-n films have been studied. The excitation spectra of CNMY-n by monitoring the emission at 612 nm (the $^5D_0$-$^7F_2$ transition of Eu^{3+}) show a strong and broad band, and a number of sharp emission lines (Figure S3). The broad band between 200-300 nm reflects the energy transfer between O^{2-} and Eu^{3+} ions, known as charge-transfer band, and the sharp lines in the range of 350-470 nm are attributed to the 4*f*-4*f* transitions of Eu^{3+} ions (^7F_J-$^5L_6$/$^5D_3$).[19] The similarity among the excitation spectra of CNMY-n implies similar structural symmetry.

The emission spectra of CNMY-n and REF-n under the excitation of 395 nm are shown in Figure 4. The transmittance spectra reveal the PSB centered at 818, 616 and 416 nm with the depth of 19%, 59% and 17% for CNMY-1, CNMY-2 and CNMY-3, respectively (Figure 4b). The PSB of CNMY-2 centered at 616 nm overlaps with the $^5D_0$-$^7F_2$ transition of Eu^{3+} at 612 nm. The effect of the PSB on the photoluminescence of CNMY-2 was monitored by normalizing the emission spectra under the $^5D_0 \rightarrow {}^7F_4$ transition at 701 nm that is far away from the PSB. As shown in Figure 4a, the PSB of CNMY-2 centered at 616 nm overlaps with the $^5D_0$-$^7F_2$ transition of Eu^{3+} at 612 nm so that the emission intensity of CNMY-2 at 612 nm is obvious weaker than that of REF-2, conforming the strong photon trapping effect due to multi-diffraction in the periodic structure.[10] Furthermore, PSB suppression on the emitters is stronger in the inside and weaker on the outside. At the same time, owing to smaller PSB depth and faraway from the $^5D_0$-$^7F_2$ transition, the emission intensities of CNMY-1 and CNMY-3 at 612 nm remain constant comparing with REF-2 and REF-3, respectively.

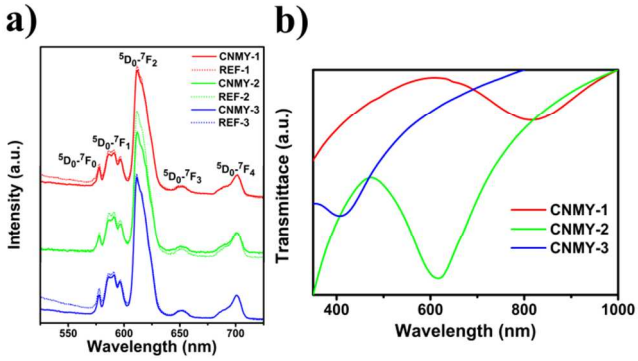

Figure 4. (**a**) Normalized emission spectra of CNMY-n and REF-n (n=1-3) recorded at λ_{ex}= 395 nm. (**b**) Transmission spectra of CNMY-n (n=1-3) with the surface normal to the beam.

The room temperature luminescent decay dynamics of CNMY-n and REF-n was monitored for the transition of $D_0 \rightarrow {}^7F_2$ upon excitation at 260 nm (Figure 5). Results show that CNMY-n has longer life time than their corresponding REF-n (Table S2). The decay curves of CNMY-n and REF-n can be best fitted by a single exponential function:

$$I(t) = I_0 e^{-t/\tau} \qquad \text{(Eq.1)}$$

where τ is the decay time constant measured at fixed wavelength, and I_0 represents the decay component. The single exponential decay of the chiral nematic mesoporous films might imply that CNMY-n contain luminescent centers with the same local density

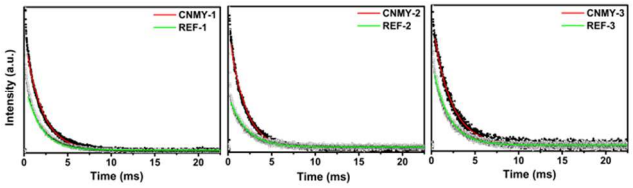

Figure 5. Room temperature photoluminescence decay curves of CNMY-n and REF-n (n=1-3) by monitoring the characteristic emissions of 612 nm at λ_{ex}=260 nm. Solid line is based on experimental data.

of state (LDOS).[16] In an ideal photonic crystal, LDOS is zero over the photonic stop band causing a band of frequencies forbidden. However, this does not happen in reality, instead, suppression of spontaneous emission takes place.[13] In general, the suppression of spontaneous emission rate in photonic crystal is attributed to the decrease of LDOS.[16] The rate of spontaneous emission in the weak oscillator-field coupling is proportional to the LDOS electromagnetic modes according to Fermi's Golden Rule.[35] The decrease of LDOS should strongly depend on the position of PSB that leads to the decrease in spontaneous emission rate. Based on above theory, the decay time constants in CNMY-2 should be the longest due to PSB overlapping with the $^5D_0$-$^7F_2$ transition, while the decay components of CNMY-1 and CNMY-3 should maintain, however, experimental data shows otherwise (Table S2).

The spontaneous emission rate is determined by the sum of radiative transition rate and the nonradiative relaxation rate. On the basis of the J-O theory, the radiative lifetime of the electric dipole transition for rare earth ions in virtual cavity model can be written as:[36]

$$\tau \approx \lambda_0 / f(ED)[(n_{eff}+2)/3]^2 n_{eff} \qquad \text{(Eq.2)}$$

where *f(ED)* is the electric dipole strength, n_{eff} is the average refractive index of the medium and λ_0 is the wavelength in vacuum. The average refractive index of the chiral nematic mesoporous CNMY-n can be expressed as:

$$n_{eff} = \phi_{air}\, n_{air} + \phi_{Y2O3} n_{Y2O3} \qquad \text{(Eq.3)}$$

where n_{eff} is inversely proportional to bulk density, namely, the greater the porosity is, the smaller of n_{eff}. As shown in Table S1, CNMY-n has similar pore volumes, hence, similar n_{eff} and emission life time between CNMY-n films. The Y_2O_3:Eu^{3+} nanoparticles in REF-n are closely packed, therefore, it can be anticipated that REF-n have greater n_{eff}, hence, greater spontaneous emission rates compared to CNMY-n. In this case, the spontaneous emission rates in the CNMY-n films are not only attributed to the variation of LDOS but also the variation of refractive index.

Angle-dependent PSB and its modulation on photoluminescence

The angle-dependent PSB and its modification on the spontaneous emission is a critical attribute of photonic crystals. The transmittance spectra of CNMY-n were collected at different incident angles with respect to the normal of the film surface. As shown in Figure 6, at normal incidence ($\theta = 0^\circ$), the PSBs of CNMY-1, CNMY-2 and CNMY-3 are at 818, 616 and 416 nm, respectively, where the PSB of CNMY-2 overlaps with the $^5D_0$-

$^7F_2$ emission of Y_2O_3:Eu^{3+}. As the incident angle increases from 0° to 60°, the PSB of CNMY-n broadens with reducing depth and the central position of the PSB shifts to shorter wavelength that fits well with Eq. 4:

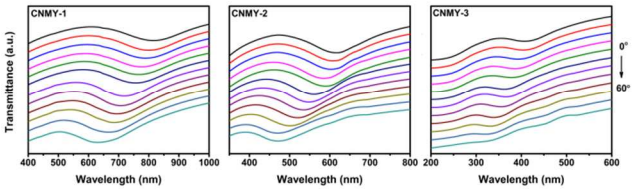

Figure 6. Transmittance spectra of CNMY-n (n=1-3) collected at different incidence angle.

$$\lambda = n_{eff} P \cdot Sin\theta \qquad \text{(Eq.4)}$$

where λ is the center wavelength of PSB, P is the helical pitch and θ is the incident angle.[37]

The angle-dependence of decay time constants of $^5D_0$-$^7F_2$ for CNMY-n films is shown in Figure 7. The result indicates that the decay time constants of $^5D_0$-$^7F_2$ are almost independent of incident angles for the CNMY-n films, confirming that the spontaneous emission rates of $^5D_0$-$^7F_2$ do not obviously vary with the location of PSB. This implies that the spontaneous emission rates of $^5D_0$-$^7F_2$ of Eu^{3+} ions cannot be readily modified by the LDOS electromagnetic modes in CNMY-n films, even though the LDOS sequentially varies with the change of the incident angle.[38]

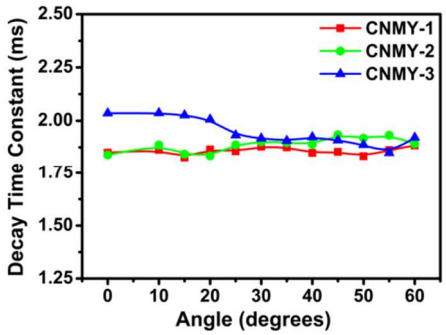

Figure 7. Dependence of the decay time constants of the $^5D_0$–$^7F_2$ transition for CNMY-n (n=1-3) at different incident angles (λ_{ex}= 395 nm)

Angle-resolved emission spectra of CNMY-n were performed and the branch ratio of the main emission line, noted as $I(^5D_0$–$^7F_2)$ /$\Sigma I(^5D_0$-$^7F_J)$ (J=0-4), was calculated as shown in Figure 8. For CNMY-3, even though the location of PSB varies with changing incident angle, the branch ratio of $I(^5D_0$–$^7F_2)$ /$\Sigma I(^5D_0$-$^7F_J)$ (J=0-4) remains constant and can be taken as a reference due to the PSB location far away from the $^5D_0 \rightarrow {}^7F_J$ transition. Furthermore, the relative branch ratio of $^5D_0 \rightarrow {}^7F_2$ at 612 nm for CNMY-2 film decreases first and approaches the minimum at 40°, and then increases again with increasing deflection angle from 40° to 60°. This observation is consistent with previous reports.[39] The emission intensity is suppressed when the emission line locates in the center of PSB, while the intensity is enhanced as the emission line locates on the edge of PSB. However, a similar result is observed in CNMY-1 with smaller branch ratio at 40° in contrast to CNMY-2, even though the location of PSB does not overlap with the $^5D_0 \rightarrow {}^7F_2$ transition with varying deflection angle. This observation implies that structural anisotropy may have strong modulation effect on the spontaneous emission rates of Eu^{3+} in chiral nematic structures.[40]

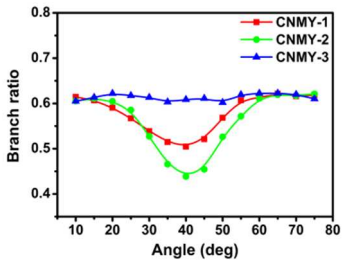

Figure 8. The intensity ratio of $I(^5D_0$–$^7F_2)/\Sigma I(^5D_0$–$^7F_J)$ (J=0–4) of CNMY-1, CNMY-2 and CNMY-3 as a function of deflection angle.

Modification of the photoluminescence of the CNMY-n films with polarized excited light

CNMY-n have novel photonic crystal structures and display different optical properties from those of three-dimensional photonic crystal structures such as opal and inverse opal likely due to structural anisotropy induced response to the polarization of light.[20, 22, 41] The emission spectra of $^5D_0$-$^7F_2$ of CNMY-n recorded under the excitation of 464 nm with unpolarized light and linearly polarized light are shown in Figure 9. Decreasing differences in the steady-state emission in the order of CNMY-1 > CNMY-2 > CNMY-3 are observed, coincide with the order of helical pitches (helical pitch: CNMY-1 > CNMY-2 > CNMY-3). It is interesting to note that the $^5D_0$-$^7F_2$ transition displays stronger intensity when excited by unpoloarized light than that by linearly polarized light for CNMY-1 and CNMY-2 while an inverse order is observed for CNMY-3. The decay time constants of CNMY-n for the $^5D_0$-$^7F_2$ transition are nearly independent of light polarization and have moderate decay time constants, confirming that the spontaneous emission rates of the $^5D_0$-$^7F_2$ transition in CNMY-n do not vary with the polarization of excited light for CNMY-n (Table S3). We conclude that the helical pitch maybe have strong modification effect on the emission of Eu^{3+} in the CNMY-n films. Increasing helical pitch leads to reduced density of state, causing an inhibition of the $^5D_0$-$^7F_2$ transition.[16, 22, 42] Different helical pitch will lead to the anisotropic properties at different levels in chiral nematic structures. We speculate that the structural anisotropy maybe play an important role in the emission spectra of Eu^{3+} in the CNMY-n films.

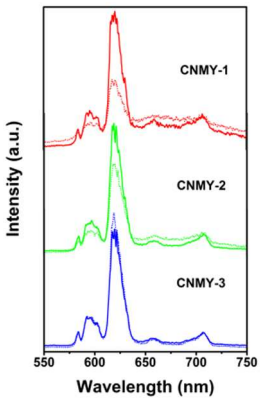

Figure 9. Normalized emission spectra of the $^5D_0$–$^7F_4$ transition of CNMY-n (n=1-3) excited by unpolarized light (solid line) and linear polarized (dotted line) light at λ_{ex}= 464 nm.

Conclusions

Free-standing luminescent films of Y_2O_3:Eu^{3+} with chiral nematic mesoporous structure and tunable optical properties have been successfully fabricated by using hard-templating approach. The chiral nematic mesoporous films afford to modulate the spontaneous emission of the Eu^{3+} ions due to the photonic crystal structures. The modulation effect on the spontaneous emission of Eu^{3+} can be attributed to the variation of density of states and anisotropic nature of the chiral nematic arrangement of Y_2O_3:Eu^{3+}. The current finding manifests the benefit of integrating luminescence, iridescence and mesoporosity into one free-standing chiral nematic film of Y_2O_3:Eu^{3+}. It opens a novel avenue for modulating the spontaneous emission of luminescent species that may be useful for developing novel optical nanodevices.

Acknowledgements

The authors are grateful to the funding agencies including the National Natural Science Foundation of China (21171067, 21373100), Jilin Provincial Talent Funds (802110000412) and Tang Aoqing Professor Funds of Jilin University (450091105161). Sincere gratitude goes to Prof. X.Y.Liu for POM imaging analysis.

Notes and references

[a] *State Key Lab of Inorganic Synthesis and Preparative Chemistry, Jilin University, 2699 Qianjin Street, Changchun 130012, China; Tel: 86 431 85168607; E-mail: yanxu@jlu.edu.cn;*
[b] *State Key Laboratory of Integrated Optoelectronics, College of Electronic Science and Engineering, Jilin University, 2699 Qianjin Street, Changchun 130012, China;*

† Electronic Supplementary Information (ESI) available: [details of any supplementary information available should be included here]. See DOI: 10.1039/b000000x/

1. Y. Akahane, T. Asano, B.S. Song and S. Noda, *Nature*, 2003, **425**, 944-947.
2. S.Y. Lin, J. Fleming, D. Hetherington, B. Smith, R. Biswas, K. Ho, M. Sigalas, W. Zubrzycki, S. Kurtz and J. Bur, *Nature*, 1998, **394**, 251-253.
3. J. H. Moon and S. Yang, *Chem.Rev.*, 2009, **110**, 547-574.
4. L. González-Urbina, K. Baert, B. Kolaric, J. Pérez-Moreno and K. Clays, *Chem.Rev.*, 2011, **112**, 2268-2285.
5. X. Dong, H. Tam and P. Shum, *Appl. Phy. Lett.*, 2007, **90**, 151113.
6. J. Broeng, D. Mogilevstev, S. E. Barkou and A. Bjarklev, *Opt. Fiber Technol.*, 1999, **5**, 305-330.
7. A. Blanco, E. Chomski, S. Grabtchak, M. Ibisate, S. John, S. W. Leonard, C. Lopez, F. Meseguer, H. Miguez and J. P. Mondia, *Nature*, **2000**, 405, 437-440.
8. L. Rindorf, J. B. Jensen, M. Dufva, L. H. Pedersen and O. Bang, *Opt. Express*, 2006, **14**, 8224-8231.
9. Y. Zhao, Z. Xie, H. Gu, C. Zhu and Z. Gu, *Chem. Soc. Rev.*, 2012, **41**, 3297-3317.
10. S. John and J. Wang, *Phys. Rev. Lett.*, 1990, **64**, 2418.
11. Z. K. Zhou, D. Y. Lei, J. Liu, X. Liu, J. Xue, Q. Zhu, H. Chen, T. Liu, Y. Li and H. Zhang, *Adv. Opt. Mater.*, 2014, **2**, 56-64.
12. T. Yoshie, A. Scherer, J. Hendrickson, G. Khitrova, H. Gibbs, G. Rupper, C. Ell, O. Shchekin and D. Deppe, *Nature*, 2004, **432**, 200-203.
13. N. Ganesh, W. Zhang, P. C. Mathias, E. Chow, J. Soares, V. Malyarchuk, A. D. Smith and B. T. Cunningham, *Nat. Nanotechnol.*, 2007, **2**, 515-520.
14. F. Zhang, Y. Wan, T. Yu, F. Zhang, Y. Shi, S. Xie, Y. Li, L. Xu, B. Tu and D. Zhao, *Angew. Chem. Int. Ed.*, 2007, **46**, 7976-7979.
15. X. Qu, H. Song, G. Pan, X. Bai, B. Dong, H. Zhao, Q. Dai, H. Zhang, R. Qin and S. Lu, *J. Phys. Chem. C*, 2009, **113**, 5906-5911.
16. P. Lodahl, A. F. Van Driel, I. S. Nikolaev, A. Irman, K. Overgaag, D. Vanmaekelbergh and W. L. Vos, *Nature*, 2004, **430**, 654-657.
17. Y. Zhu, W. Xu, H. Zhang, W. Wang, S. Xu and H. Song, *J. Phys. Chem. C*, 2012, **116**, 2297-2302.
18. X. Qu, H. K. Yang, B. K. Moon, B. C. Choi, J. H. Jeong and K. H. Kim, *J. Phys. Chem. C*, 2010, **114**, 19891-19894.
19. X. Qu, B. Dong, G. Pan, X. Bai, Q. Dai, H. Zhang, R. Qin and H. Song, *Chem. Phys. Lett.*, 2011, **509**, 33-36.
20. K. E. Shopsowitz, H. Qi, W. Y. Hamad and M. J. Maclachlan, *Nature*, 2010, **468**, 422-425.
21. D. Katsis, D. Kim, H. Chen, L. Rothberg, S. Chen and T. Tsutsui, *Chem. Mater.*, 2001, **13**, 643-647.
22. S. Chen, D. Katsis, A. Schmid, J. Mastrangelo, T. Tsutsui and T. Blanton, *Nature*, 1999, **397**, 506-508.
23. A. Bobrovsky, K. Mochalov, V. Oleinikov, A. Sukhanova, A. Prudnikau, M. Artemyev, V. Shibaev and I. Nabiev, *Adv. Mater.*, 2012, **24**, 6216-6222.
24. K. L. Woon, M. O'Neill, G. J. Richards, M. P. Aldred and S. M. Kelly, *Phys. Rev. E*, 2005, **71**, 041706.
25. K.-C. Shin, F. Araoka, B. Park, Y. Takanishi, K. Ishikawa, Z. Zhu, T. M. Swager and H. Takezoe, *Jpn. J. Appl. Phys.*, 2004, **43**, 631.
26. H. Qi, K. E. Shopsowitz, W. Y. Hamad and M. J. MacLachlan, *J. Am. Chem. Soc.*, 2011, **133**, 3728-3731.
27. T.D. Nguyen, W. Y. Hamad and M. J. MacLachlan, *Adv. Func. Mater.*, 2014, **24**, 777-783.
28. G. Chu, J. Feng, Y. Wang, X. Zhang, Y. Xu and H. Zhang, *Dalton T.*, 2014, DOI: 10.1039/c4dt00662c.
29. S. Beck-Candanedo, D. Viet and D. G. Gray, *Langmuir*, 2006, **22**, 8690-8695.
30. K. E. Shopsowitz, A. Stahl, W. Y. Hamad and M. J. MacLachlan, *Angew. Chem. Int. Ed.*, 2012, **51**, 6886-6890.
31. D. Zhao, J. Sun, Q. Li and G. D. Stucky, *Chem. Mater.*, 2000, **12**, 275-279.
32. T. I. Seiichi Kondo, Ikuo Abe, *Adsorption Science*, Chemical Industry Press, 2nd edn., 2006.
33. T. Lenau and M. Barfoed, *Adv. Eng. Mater.*, 2008, **10**, 299-314.
34. F. Saeva, P. Sharpe and G. Olin, *J. Am. Chem. Soc.*, 1973, **95**, 7656-7659.
35. N. Vats, S. John and K. Busch, *Phys. Rev. A*, 2002, **65**, 043808.
36. C.K. Duan, M. F. Reid and Z. Wang, *Phys. Lett. A*, 2005, **343**, 474-480.
37. H. de Vries, *Acta Crystallogr.*, 1951, **4**, 219-226.
38. X.H. Wang, R. Wang, B.Y. Gu and G.Z. Yang, *Phys. Rev. Lett.*, 2002, **88**, 093902.
39. W. Wang, H. Song, X. Bai, Q. Liu and Y. Zhu, *Phys. Chem. Chem. Phys.*, 2011, **13**, 18023-18030.
40. A. Ortigosa-Blanch, J. Knight, W. Wadsworth, J. Arriaga, B. Mangan, T. Birks and P. S. J. Russell, *Opt. Lett.*, 2000, **25**, 1325-1327.
41. M. D. Turner, M. Saba, Q. Zhang, B. P. Cumming, G. E. Schröder-Turk and M. Gu, *Nat. Photonics*, 2013, **7**, 801-805.
42. A. L. Rodarte, C. Gray, L. S. Hirst and S. Ghosh, *Phys. Rev. B*, 2012, **85**, 035430.

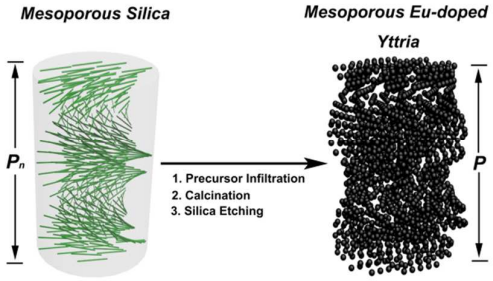

Hard templating of mesoporous chiral nematic luminescent films of Y_2O_3:Eu^{3+} with tunable optical properties and novel emission spectra.